

*Annual Review of Condensed Matter Physics*  
**Physics of Human Crowds**

Alessandro Corbetta<sup>1</sup> and Federico Toschi<sup>1,2</sup>

<sup>1</sup>Department of Applied Physics and Science Education, Eindhoven University of Technology, Eindhoven,

The Netherlands; email: a.corbetta@tue.nl, f.toschi@tue.nl

<sup>2</sup>Consiglio Nazionale della Ricerca-IAC, Rome, Italy

**ANNUAL REVIEWS CONNECT**

[www.annualreviews.org](http://www.annualreviews.org)

- Download figures
- Navigate cited references
- Keyword search
- Explore related articles
- Share via email or social media

Annu. Rev. Condens. Matter Phys. 2023. 14:311–33

First published as a Review in Advance on November 30, 2022

The *Annual Review of Condensed Matter Physics* is online at [commatphys.annualreviews.org](http://commatphys.annualreviews.org)

<https://doi.org/10.1146/annurev-conmatphys-031620-100450>

Copyright © 2023 by the author(s). This work is licensed under a Creative Commons Attribution 4.0 International License, which permits unrestricted use, distribution, and reproduction in any medium, provided the original author and source are credited. See credit lines of images or other third-party material in this article for license information.

### Keywords

human crowd dynamics, active matter, social physics, emergent phenomena, observational experiments, pedestrian flows

### Abstract

Understanding the behavior of human crowds is a key step toward a safer society and more livable cities. Despite the individual variability and will of single individuals, human crowds, from dilute to dense, invariably display a remarkable set of universal features and statistically reproducible behaviors. Here, we review ideas and recent progress in employing the language and tools from physics to develop a deeper understanding about the dynamics of pedestrians.

## 1. INTRODUCTION

Understanding the dynamics of human crowds has deep implications for the quality of our leisure time (e.g., while visiting museums or exhibits), for the efficiency of our daily business (e.g., when shopping in a supermarket or commuting in a metro station), and even for our personal safety (e.g., when walking in large crowds or during emergency evacuations). The behavior of human crowds is something we are all familiar with, from our daily experience, and still crowds can display a wide range of challenging and surprising behaviors. Due to individual variability, individual will, and the different behaviors that we adopt in different environments, the very idea of being able to model, let alone predict, the dynamics of human crowds seems a hopelessly daunting task. The dynamics of human crowds has often been related to the flow of fluids, and human crowds have even been dubbed thinking fluids (1). More specifically, one can see human crowds as a special branch of active matter physics, where the active agents, instead of being bacteria, birds, or the like, are human beings (2).

Due to the difficulties in acquiring measurements or conducting experiments on human crowds, it is understandable that much attention has been given to the development of mathematical and numerical models (3–6), based on more or less reasonable physical and behavioral assumptions. However, it is important to stress that real human crowds will invariably behave differently from these abstract and theoretical models.

In this review, we address recent progress in the understanding of human crowd dynamics while focusing on models and behaviors that have been experimentally verified. Given the difficulties of performing measurements in real-life settings, in conjunction with individual privacy as well as ethical aspects, an important role has been played by laboratory experiments, whereby crowds of voluntary participants are instructed to accomplish specific tasks, and accurate laboratory recordings are at the basis of quantitative insights into the dynamics. Although laboratory setups allow for the design of specific and well-controlled experiments (e.g., pedestrians leaving a room via an assigned door, sustained presence of counterflowing crowds in narrow corridors), they come at the price of a subtle and often difficult to quantify psychological influence on the pedestrians. In fact, participants in the experiments receive prior instructions on their duties, which invariably influence their behavior.

As in the case of fluid flows, physical descriptions of a crowd depend on the length and timescales of observation. For this reason, we discuss the dynamics of human crowds at five different scales that are sketched in **Figure 1**. Starting from the coarsest description, addressing very large length and timescales, and zooming in progressively to include finer and finer details, these five scales are the following:

- Supermacroscopic scale. At this level, the crowd is described in terms of “equations of state” that connect different macroscopic quantities, such as the average velocity and density. No spatial description or resolution is available, and the dynamics over a complex environment (e.g., a city) can be described as dynamics over a graph.
- Macroscopic scale. The crowd is described as a continuum; no individual is resolved, but space- and time-dependent density and velocity fields represent a coarse-grained description of a crowd. This level of description clearly shares some similarity with hydrodynamics.
- Mesoscopic scale. The dynamics of individual pedestrians is described in terms of few degrees of freedom (e.g., position, orientation) and in a statistical sense. However, individual pedestrians are thought of as single discrete entities. This description shares similarities with the kinetic theory of gases.

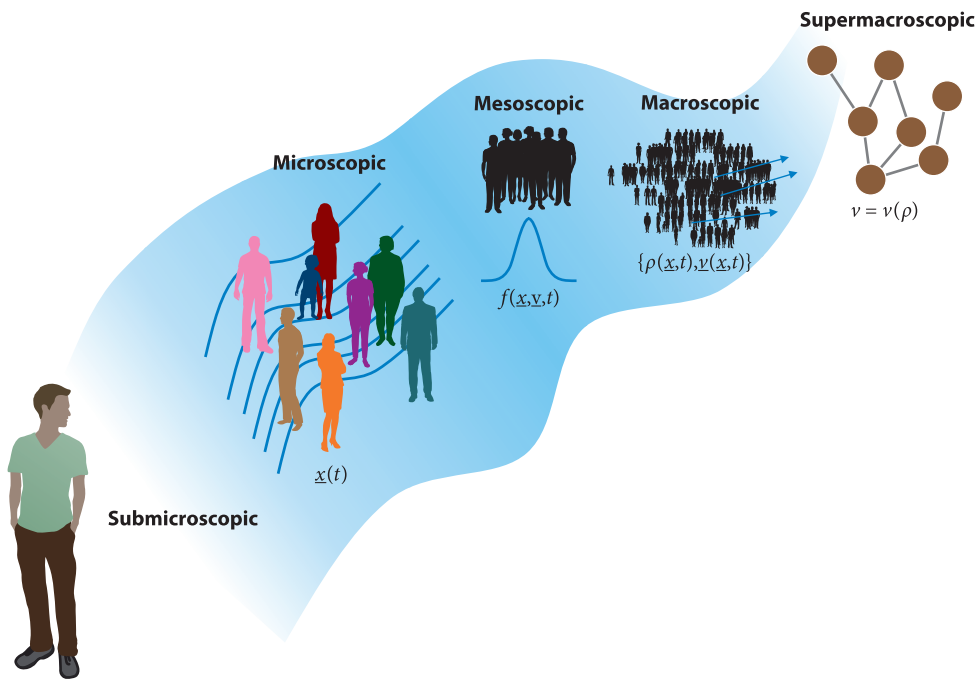


**Figure 1**

Human crowds can be observed at different length and timescales, here called submicroscopic, microscopic, mesoscopic, macroscopic, and supermacroscopic, disclosing different phenomenological behaviors and calling for different mathematical and physical descriptions. These entail as a function of the scale, respectively, (*submicroscopic*) full detail on individuals (e.g., height, orientation of head/shoulders, presence of backpacks); (*microscopic*) individual positions; (*mesoscopic*) probabilities of individual states; (*macroscopic*) continuous fields as density and velocity; and (*supermacroscopic*) integral or average quantities (density, fluxes, velocities) defined on representative or simplified scenarios (graphs).

- **Microscopic scale.** This scale resolves single individuals, typically involving centimeter accuracy in space and tenths-of-a-second resolution in time. Such description shares close similarities with the molecular dynamics approach to gases.
- **Submicroscopic scale.** This is the scale of the single individual with observables beyond the position as a function of time. By observing a crowd at this level, one can detect features such as the orientation of the body and of the head, attitude, and the presence of backpacks and trolleys. At this scale, the details of the interaction with other pedestrians, as well as with geometrical elements such as chairs, tables, and walls, are fully visible.

The dynamics of human crowds, similar to that of gases and active matter, displays emerging complexity at the largest length scales and timescales, which stresses the importance of considering the right level of description. Just as an example, if one is interested in individual-level dynamics, a microscopic description will be required. On the other side, focusing on a description at too fine of a scale may obscure the phenomenology, which is easily observable at larger scales. In this respect, focusing on the highest-level description is not only often more efficient from an analytical or numerical point of view but, most importantly, allows one to focus on the relevant phenomena (e.g., the macroscopic density waves in Reference 7).

In the following, we focus on some of the phenomenological aspects of crowd dynamics that we consider most relevant and discuss them in connection with a pertinent level of description

## GAINING INFORMATION ON PEDESTRIAN DYNAMICS

Simulation, laboratory, and naturalistic experiments have been employed to establish fundamental and technology-oriented knowledge on pedestrian dynamics. As dedicated computer-vision technology emerged, qualitative analyses unlocked by simulations studies have been integrated with systematic data acquisition campaigns:

- Laboratory investigations, discussed in the literature since the late 1950s, blossomed around the beginning of the millennium and hinge on participants walking within artificial setups following the experimenter's indications. Colored vests and helmets are generally employed to ease and improve the quality of tracking (e.g., 8, 9). While allowing an accurate and complete definition of the experimental settings [e.g., density (10)], geometry (11, 12), and sentiment (13), the laboratory investigations are limited in statistics (owing to the necessary involvement of volunteers and the limited time span of the experiments as well as the artificial conditions that could potentially induce psychological biases in the volunteers).
- Naturalistic experiments allow potentially limitless data collection (via 24/7, 365-days-per-year data acquisition) and, thus, the possibility of resolving pedestrian dynamics beyond average behaviors. After the 2010s, renewed technologies, sometimes based on machine-learning techniques, unlocked accurate tracking in completely naturalistic settings even in real time (14–17). By contrast, real-life pedestrian venues generally entail a plethora of different crowd scenarios widely varying in space and time (low/high density, uni-/multidirectional flows, heterogeneous presence of groups, etc.). Occurrences of similar crowd scenarios need to be selected and aggregated *a posteriori* (cf. a graph-based approach; 18, 19) for statistical analyses of different scenarios.
- Mathematical and physics models have been continually improved thanks to the input from laboratory and naturalistic studies. However, it must be stressed that even earlier models, though qualitative in nature (3, 20, 21), were instrumental in exploring key aspects of the phenomenology of human crowds and in supporting the idea that a number of observed dynamics could be modeled in quantitative terms.

These three approaches are complementary and often integrated; experimental data, collected in either an artificial or a real-life environment, are beginning to be widely used to validate and calibrate simulation models.

(micro, meso, or macro). Along with a brief analysis of the phenomenology (see the sidebars titled Gaining Information on Pedestrian Dynamics and titled Experimental Measurements and Pedestrian Tracking), we address some mathematical and physics tools that can be used for the study and modeling of the observed dynamics.

## 2. SUPERMACROSCOPIC SCALE

When dealing with vast areas and crowd dynamics in typical flow conditions, it may be enough to describe the geometry in terms of a network of nodes connected by links. The nodes may correspond to sources or destinations (e.g., entrance/exit doors in a train station) or intermediate waypoints that mark positions where the flow may branch toward different nodes. The crowd description should incorporate conservation laws at internal nodes and the fact that the flux of pedestrians through each link depends on the local density through the link. In some respects, this approach resembles the thermodynamic-level description of a gas, where only macroscopic quantities such as pressure, temperature, and density are used to model the gas and are connected via an equation of state. In this case, the relevant relation is the connection between the average walking speed (in a link)  $\langle v \rangle$  and the density  $\rho$ :

$$\langle v \rangle = f(\rho). \quad 1.$$

## EXPERIMENTAL MEASUREMENTS AND PEDESTRIAN TRACKING

Different methods to acquire experimental pedestrian dynamics measurements have been developed, offering different levels of accuracy, autonomy, and privacy:

**People counters.** Supermacroscopic measurement approaches, aimed at fundamental diagram-like relations, have existed since the late 1950s. In fact, quantities such as global density, fluxes, and average velocities can be estimated manually from field observations (e.g., 22, 23). Manual techniques have increasingly been replaced by automatic tools. These include high-precision optical tracking, which emerged in the early 2000s (e.g., 24), allowing not only improvement of supermacroscopic estimates, thanks to larger statistics, but also investigation of microscopic behavior (see Tracking, below). Lower-resolution methods based on (anonymous) tracking of radio beacons have also seen greater and greater adoption. Radio-trackable devices have been explicitly supplied to pedestrians (especially in the context of museum visitors tracking, e.g., bare Bluetooth beacons in Reference 25 or even smart educational devices in Reference 26). Alternatively, self-advertisement signals of mobile phone Bluetooth or Wi-Fi adaptors have been employed [e.g., to reveal intermittent motion patterns within the audience of concerts (27) or to determine routing choices (28)].

**Techniques inspired by fluid dynamics.** Methods to measure macroscopic-scale pedestrian dynamics have also been developed. In the spirit of traditional Eulerian image velocimetry in fluid mechanics (29) or (block matching) optical flow (30), subsequent (color) snapshots of the experimental area have been used to derive Eulerian velocity fields,  $\mathbf{v}(\mathbf{x})$  (cf. Equation 2; 7, 31–33). Estimations of macroscopic density fields,  $\rho(\mathbf{x})$ , have, instead, usually been performed by individual (i.e., microscopic) head counting, although one-shot approximations have also been proposed (e.g., 34).

**Tracking.** Microscopic-scale measurements of individual trajectories are a recent achievement, especially in real-time, real-life settings. Microscopic measurements usually involve alternating a localization phase, in which individual positions are estimated from optical signals (usually color or depth) and a point-tracking phase in which positions in different frames are linked together to build trajectories. Color footage, generally aided with markers, has been extensively employed in laboratory experiments (8, 35–37), whereas overhead depth sensors have been used for real-life campaigns (14, 16, 38), possibly at high densities (39).

**Submicroscopic measurements.** The measurement of individual degrees of freedom finer than positions is receiving more and more attention as technology evolves. Elements such as gestures, presence of trolleys/bags, or heterogeneous body size or age can have great impact in the dynamics. Body rotation is a fine-scale individual feature that has been successfully extracted from video or depth feeds. Video-based analyses typically required dedicated markings on the shoulders to facilitate manual data extraction (40). In the case of real-life depth feeds, supervised machine-learning estimators have been used to automate measurements (41). In the last case, to prevent labor-intensive data annotations, the typical (but not exact) orthogonality between velocity and shoulder line has been employed to create machine-learning training data. Body rotation has also been extracted thanks to dedicated inertial measurement units attached to individual bodies (35). The same principle, applied to entire vests, has been used to obtain complete locomotion measurements of individual body parts (42).

Such a relation  $f$  is called a macroscopic fundamental diagram and represents the fact that the average walking speed is a monotonically decreasing function of the density. This occurs with a certain degree of universality across different forms of transportation (e.g., walking, cycling, driving; 43). Fundamental diagrams are also often reported as relationships between the crowd flux, i.e., the (average) number of pedestrians per unit time per unit area, and density (**Figure 2**).

An example of a fundamental diagram was proposed by Weidmann (44), after pioneering work started in the late 1950s (22, 23). Extensive experimental and numerical work has been conducted in order to investigate the dependence of the fundamental diagram on a number of parameters like the transversal width of the link [37; including the single-file limit (46)], cultural origin (47),

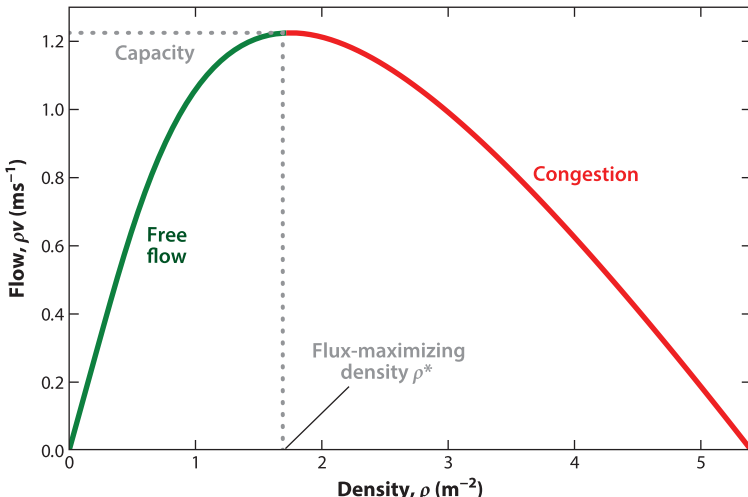


**Figure 2**

Fundamental diagram for the pedestrian flux, i.e., the relationship between local density ( $x$  axis, measured in pedestrians per reference area) and the pedestrian flux ( $y$  axis, measured in pedestrians crossing an interface, per unit interface length per unit time). Numerical values and fitting refer to the metastudy (44) in which the functional form  $\rho v(\rho) = \rho v_0 \{1 - \exp[-\gamma(\rho^{-1} - \rho_{\max}^{-1})]\}$  was proposed ( $v_0 = 1.34 \text{ ms}^{-1}$ ,  $\rho_{\max} = 5.4 \text{ m}^{-2}$ ,  $\gamma = 1.913 \text{ m}^{-2}$ ). Figure adapted from Reference 45 (CC BY 4.0).

and physique (15), but also environmental elements such as background music (48; see also the review in Reference 49).

One key aspect associated with the reduction of the average walking speed as the density increases is that the crowd flux,  $\rho(v)$ , admits an optimal density  $\rho^*$ , attaining the transport capacity of the link. The reason why the flux versus the density presents a maximum is nontrivial and is deeply connected with the intra- and interpersonal variability of walking speeds (see also 10). Indeed, supposing that each pedestrian would perfectly and constantly walk with the same speed, the flux should just be linearly growing with the density up to capacity, i.e., the maximal achievable density level. The presence of fluctuations, instead, leads to “repulsive collisions” between walking pedestrians. This is similar to what happens with vehicular traffic flows or to the formation of shocks for the Burgers equation in fluid dynamics (50).

The generalization from a single link to a network of links allows more and more faithful, yet coarse, descriptions of the dynamics (51). In this perspective, corrected forms of fundamental diagrams have been proposed that entail bidirectional (“counterflowing”) traffic within a link (38, 52; for the bidirectional equivalent of a link capacity, see 45), turns (53), intersections (11, 54), and junctions (55). Finally, the fundamental diagram has been computed even for high velocities by tracking escaping pedestrians in the context of the tradition of the Running of the Bulls in Pamplona, Spain (33).

### 3. MACROSCOPIC SCALE

An obvious step forward in incorporating geometrical features consists of considering all space positions  $\mathbf{x} = (x, y)$  and describing the crowd via macroscopic fields such as the local density  $\rho(\mathbf{x}, t)$  and velocity  $\mathbf{v}(\mathbf{x}, t)$ . This approach shares clear similarities with the fluid dynamics description of gases, in which the continuum macroscopic fields come from considering a large-enough volume including sufficiently many gas molecules. In the case of crowds, this approach is meaningful only when the density and other macroscopic observables are well defined, i.e., at a spatial scale

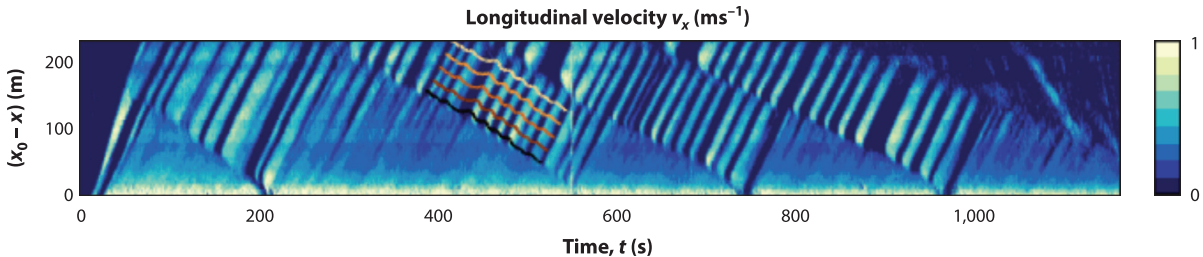


**Figure 3**

By using particle image velocimetry techniques, it is possible to study the velocity evolution of crowds at the macroscopic level. Shown here is the dynamics of the propagation of linear (nondispersive) velocity waves at the start of the Chicago Marathon. Figure adapted with permission from Reference 7; permission conveyed through Copyright Clearance Center, Inc.

several times larger than the size of a single individual, or when the ratio between the mean displacement and the typical system size (Knudsen number) is small, and in the presence of sufficient pedestrians. In these conditions, the hypothesis of continuity for the pedestrian mass holds in the formula

$$\frac{\partial \rho(\mathbf{x}, t)}{\partial t} + \nabla \cdot [\mathbf{v}(\mathbf{x}, t)\rho(\mathbf{x}, t)] = 0. \quad 2.$$

This coarse-grained description is still rather limited for what concerns the statistical fluctuations, as it describes the crowd via low-order hydrodynamic moments (e.g., density and possibly momentum, angular momentum, “temperature”). The connection with experimental observations can be made via the analysis of video camera recordings, e.g., employing techniques that resemble particle image velocimetry (PIV) and other, similar techniques ordinarily employed in experimental fluid mechanics (31). By observing crowds at this scale, it is possible to study instantaneous and average flows as well as the dynamics of density waves. One notable application of this approach is presented in Reference 7, which applied PIV techniques (29) in order to experimentally measure the velocity field of a crowd at the start of a marathon (**Figure 3**). The density requirements make mass gatherings an ideal candidate for macroscopic analyses, e.g., at the Holy Mosque of Makkah, Saudi Arabia, where stop-and-go wave dynamics as well as the presence of intermittent, irregular, mass displacements (dubbed crowd turbulence; see the sidebar titled Phenomenology of Crowd Dynamics) were observed (74).

Equation 2 defines an evolution model for the pedestrian density only when coupled with a suitable velocity field. A well-studied and physically meaningful option entails velocity fields allowing pedestrians to reach a known destination in minimum time (for a review on modeling alternatives, see Reference 3). Assuming a fundamental diagram relation between density and velocity (Equation 1) to hold locally in space,  $|\mathbf{v}(\mathbf{x})| = f[\rho(\mathbf{x})]$ , such a velocity field satisfies the eikonal equation

$$\begin{cases} \mathbf{v}(\mathbf{x}) = f^2[\rho(\mathbf{x})] \nabla \phi(\mathbf{x}), \\ |\nabla \phi(\mathbf{x})| = \frac{1}{f[\rho(\mathbf{x})]}, \end{cases} \quad 3.$$

where the scalar field  $\phi = \phi(\mathbf{x})$ , also dubbed action in the Hamilton–Jacobi formalism (75), encodes the remaining travel time to the destination (see Section 4.4). Equations 2 and 3, whose unknown is  $\phi$ , define the so-called Hughes model. In its original formulation, the Hughes model also included a discomfort function, usually indicated as  $g(\rho)$ , appearing as a prefactor of the term  $\nabla \phi(\mathbf{x})$  (1).

## PHENOMENOLOGY OF CROWD DYNAMICS

Emerging complexity is an ubiquitous feature in human crowd dynamics. As density increases, the simple small-scale interaction between pedestrians leads to a transition to order when complex large-scale spatiotemporal (possibly metastable; 10) patterns emerge, in connection with the anticipation capabilities of pedestrians (56–58). At higher densities, pedestrians are more constrained, they move in a more correlated fashion, and large-scale crowd patterns can even disastrously influence individual dynamics (32). This leads, e.g., to lane formation, when, in a corridor, at increasing density, two lanes flowing in opposing directions spontaneously form (9, 10, 59; **Figure 4**). Pedestrian interactions also lead to complex temporal patterns, such as intersecting flows (11, 54). When walking paths intersect, different types of behavior can emerge. At low density, the chance of collision is small and pedestrians mostly maintain the same walking pattern, occasionally changing their path (17). However, at higher densities, the crossing paths interfere considerably, and pedestrians will have to modify their path or speed up or slow down to avoid collisions. The fundamental diagram is an empirical relation providing the average walking speed as a function of few selected crowd parameters, typically the local density (46, 47, 49). Starting from the free average walking speed, as the crowd density increases, the average velocity decreases, approximately linearly, to eventually vanish. The average walking speed can be influenced by several additional factors (e.g., composition, calm or nervous state of a crowd). Walking biomechanics includes knowledge of gait, speed, shoulder orientation, and swinging (41, 62). The orientation of shoulders plays a particularly important role at higher densities and during evacuation through an exit (63). Granularity (excluded volume effects) has a key role at high densities (64). Clogs can form when the local density exceeds a critical threshold, which typically occurs during evacuations or in intermittent flows (13) through a constriction. Additionally, increasing crowd vigor leads to the faster-is-slower effect (20), entailing reduced flows due to more frequent clogs (65) (**Figure 5**). The zipper effect has been proposed for the intercalated formation of shoulder-to-shoulder lanes in narrow bottlenecks (66, 67). Crowd heterogeneity refers to the crowd composition, i.e., the percent of commuters, tourists, or students. These different groups, having different objectives, will display different behaviors (e.g., walking at different speeds), being more or less familiar with the environment. Social group dynamics is also extremely relevant to quantitatively understand the dynamics of crowds, as it is estimated that around 70% of pedestrians in a crowd are in social groups (68, 69). Ownership in a social group can significantly alter the dynamics of an individual pedestrian. Furthermore, group shape can change according to the flow conditions (70). In one-directional crowd flows, at increasing density, traffic jams may form and dissolve rapidly, which is visible via the formation of density stop-and-go waves (7) (**Figure 3**). Pedestrians tend to minimize some sort of discomfort, making pedestrian dynamics a nontrivial utility maximization process (71, 72). One relevant utility is the estimated time to destination, possibly taking into account the (decreased) walking speed due to (increased) local density. This is reminiscent of Fermat's principle, used in optics. The Braess paradox is the counterintuitive phenomenon for which adding one or more routes to a network can sometimes have a detrimental effect, decreasing the overall flow (73).

## 4. MESOSCALE SCALE

An intriguing level of description for the dynamics of human crowds is the mesoscopic level. Here, pedestrians are not described individually but at a statistical level. The type of physics and methods for describing the dynamics are closely inspired by the kinetic theory of gases, in which gas molecules are described not individually but in terms of probabilities that evolve according to equations such as the Boltzmann equation (76).

### 4.1. Cellular Automata Models

Cellular automata (CA) describe the dynamics of particles moving in discrete time steps between neighboring locations in regular 2D meshes (square or, less commonly, hexagonal; 77) and can

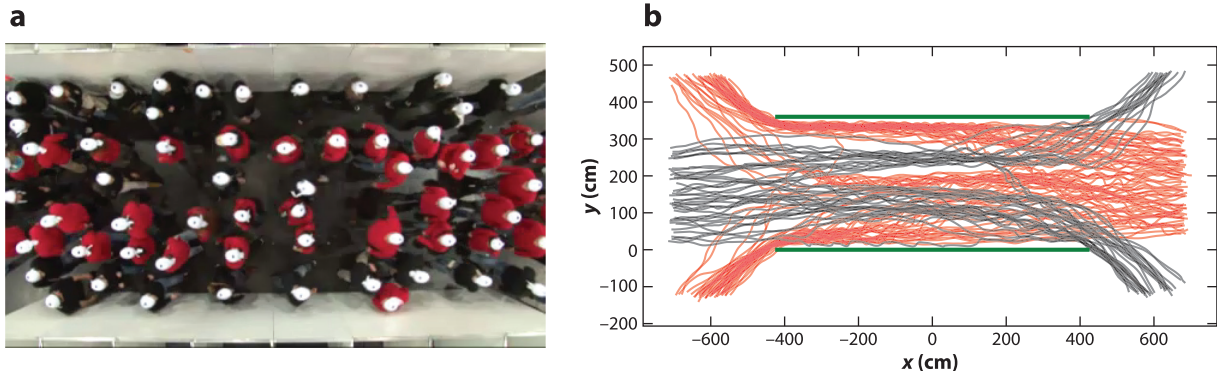


**Figure 4**

Emergence of metastable lanes in the presence of a pedestrian counterflow. Lanes emerge as pedestrians tend to tail those walking in front of them to minimize conflicts with individuals moving in the opposite direction. This scenario has been part of the Hermes Laboratory investigation (Esprit Arena, Düsseldorf, Germany). Figure adapted from Reference 59, reproduced from data sets. The data sets are publicly available (60) at the Pedestrian Dynamics Data Archive (61).

approximate complex emerging dynamics (78). CA-based treatment of pedestrian dynamics was pioneered at the beginning of the century (21, 79), on the basis of the success of analogous methods to analyze vehicular traffic (see references in 21). CA have been extensively employed in other fields of physics, for example, to describe the dynamics of fluids (80), as well as in mathematics and computer science.

Common approaches to define CA for crowd dynamics involve the definition of floor fields. Superimposing large ensembles of pedestrian trajectories to a floor, discretized in 2D cells, one can, e.g., compute the transition probabilities,  $\mathcal{P}(\mathbf{c}|\mathbf{c}')$ , to move from the generic cell  $\mathbf{c}' = (i', j')$  to a neighboring cell  $\mathbf{c} = (i, j)$  (e.g., 81). Such a floor field can naturally account for the avoidance of obstacles. Additionally, the probabilities can be computed for a given level of crowdedness (average density) and at specific moments in time (rush hour, weekend, etc.). In this way, one can statistically learn the floor field under different conditions; therefore, the probabilities  $\mathcal{P}$  have to be thought of as being dependent on these additional factors.

CA models address density limits by allowing up to one particle per cell. As the particle positions get updated in parallel, conflicts can arise owing to multiple particles targeting the same destination cell; in those cases, the update is typically chosen via a probabilistic rule (21, 82). CA models have been used, for instance, to predict the instability of balanced counterflows (see 83, including validation against dense flow data) and to study anticipation effects (58). A comparison between CA models and microscopic, force-based models (Section 5) has also been performed, e.g., in the context of evacuation (84).

## 4.2. Path Integral

More generally, the walking dynamics of pedestrians is naturally described in terms of their trajectories,  $\gamma : t \mapsto \mathbf{x}(t)$ , and an experimental observation of a crowd can be considered a statistical sampling of the relative probability,  $\mathcal{P}[\gamma]$ , of observing a path,  $\gamma$ , out of all possible paths,  $\Gamma$ . The probability density can be formally written as (85)

$$\mathcal{P}[\gamma] \mathcal{D}\gamma = \frac{1}{Z} e^{-S[\gamma]} \mathcal{D}\gamma, \quad 4.$$

where  $S[\gamma]$  is an action functional,  $\mathcal{D}\gamma$  is the formal (infinite) measure over all the trajectories (for an example of the formal construction, see 86), and  $Z = \int e^{-S[\gamma]} \mathcal{D}\gamma$  is a normalization constant.

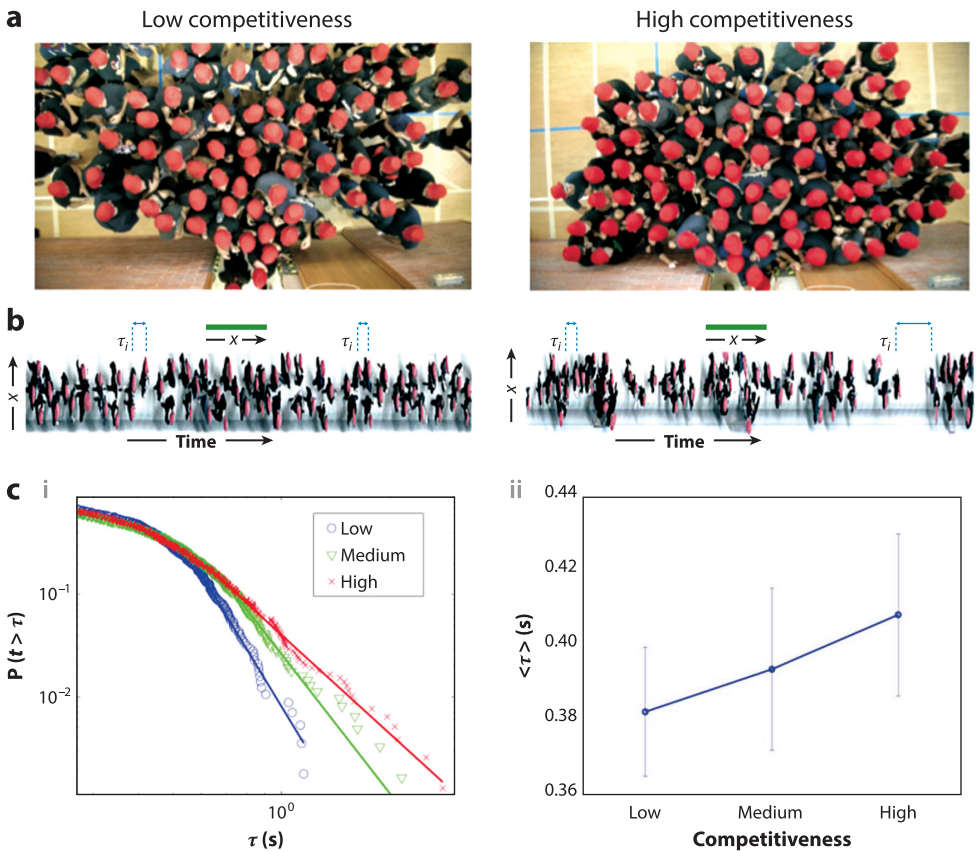


**Figure 5**

Experimental investigation of the egress of a crowd through a narrow door (69 cm). (a) Overhead snapshots of the experimental location. Participants have been instructed to act with a low or high level of competitiveness to cross through the door. (b) Spatiotemporal diagrams. Red helmets support the tracking process. (c, i) Different levels of competitiveness yield different dynamics, monitored here in terms of the time lapses,  $\tau$ , between two consecutive pedestrian crossings with survival statistics  $P(t \geq \tau)$ . Intermittent clogging yields power-law scaling. (c, ii) Average  $\tau$  as a function of the competitiveness level. As a reflection of the faster-is-slower effect, higher competitiveness in the systems (and thus higher driving force to the door) yields larger time lapses and, therefore, lower fluxes. Figure adapted with permission from Reference 65; copyright 2015 American Physical Society.

The knowledge of the action functional  $S[\gamma]$  should be considered, as in (statistical) field theory, as the knowledge of the theory, allowing computation of all statistical observables (e.g., 85). At variance with standard quantum and statistical field theories, here the action functional  $S[\gamma]$  is not known or not easily derivable from fundamental physics principles. However, one may attempt to sample the action functional from the data, seeking some guidance from possible analytical models. These data-driven semianalytical models could allow the incorporation of comprehensive knowledge of the statistical properties of pedestrian dynamics in different contexts, disclosing relevant insights.

The probabilistic weight from Equation 4 is dominated by those trajectories in the neighborhood of the local minimizers of  $S[\gamma]$ . Assuming that the action functional is known, it is possible to use it to compute all the minimizers that would represent the most typical or common pedestrian

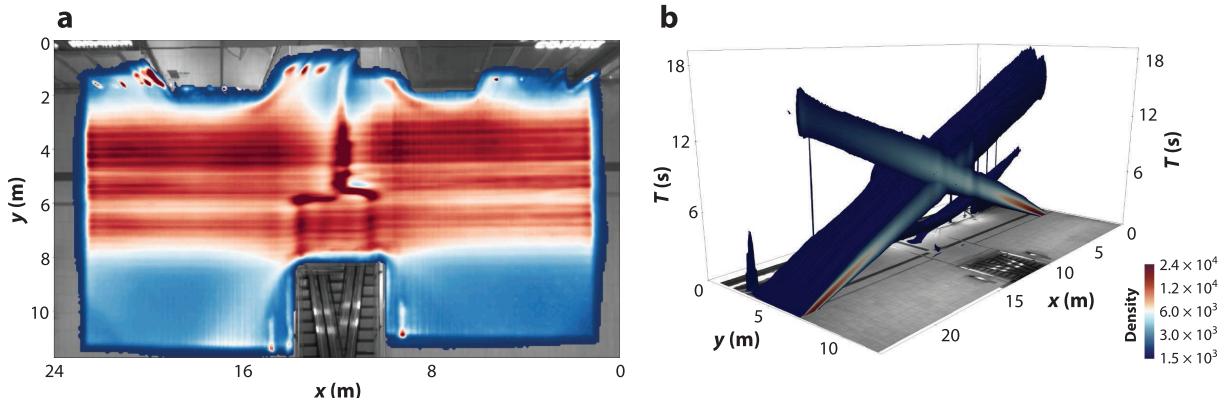


**Figure 6**

Two representations of the pedestrian dynamics in the main walkway of a train station in the Netherlands. (a) A classical heatmap (Equation 10) shows the spatial positions where pedestrians walk most frequently. This representation neglects individual dynamics, focusing on position distributions. (b) A space-time heatmap (Equation 12), in which time is reported on the vertical axis, includes temporal patterns showing the presence of opposite walking directions. For the sake of readability, only regions with a probability higher than a given threshold (see the legend) are visualized. Heterogeneity in walking speeds is reflected in the spread of probable positions as time advances. Original content courtesy of by C.A.S. Pouw.

behaviors. By numerically sampling the action functional and numerically finding these minimizers, one could therefore highly simplify the complex dynamics of millions of individual trajectories into the most relevant usage modes (with associated probabilities; **Figure 6**).

In addition, to provide an effective way to identify the most relevant usage modes, Equation 4 allows the possibility of evaluating space-time correlations of trajectories, of arbitrary orders, via functional derivatives of the momentum-generating functional  $Z[J] = \int e^{-S[\gamma]+J\gamma} \mathcal{D}\gamma$  (85). In particular, it allows one to compute the expectation value of any possible observable,  $O$ , built from a trajectory  $\gamma$  over the full set of trajectories  $\Gamma$ :

$$\langle O[\gamma] \rangle_{\Gamma} = Z^{-1} \int e^{-S[\gamma]} O[\gamma] \mathcal{D}\gamma. \quad 5.$$

Although the path-integral description discussed so far refers to the probability of the path of a single pedestrian in a crowd, this formalism could be generalized to describe the joint probability of an arbitrary number of pedestrian trajectories, something that we do not discuss further here.

It is worth stressing that though the path-integral formulation is general enough to encompass the most complex pedestrian behaviors, in simple cases one can build mathematical models for the action functional. This is the case for the simple Langevin model, discussed in Section 5, which describes pedestrian dynamics in the diluted limit, such as people walking alone or when their distance to other individuals is sufficiently large. Under these conditions, and when a pedestrian walks along a straight path, the dynamics can be modeled as that of an active Brownian particle, which yields the following action, also referred to as an Onsager–Machlup functional (e.g., 87):

$$S[\gamma] = \int_{t_i}^{t_f} dt \left[ \frac{1}{2\sigma_x^2} \left( \dot{u} + \frac{\partial \Phi_u}{\partial u} \right)^2 + \frac{1}{2\sigma_y^2} \left( \dot{v} + \frac{\partial \Phi_v}{\partial v} + \frac{\partial V}{\partial y} \right)^2 \right]. \quad 6.$$

Here,  $u = \dot{x}$  indicates the walking velocity along the longitudinal direction of the path (parallel to the  $x$  axis);  $v = \dot{y}$  is the transversal velocity (parallel to the  $y$  axis);  $\Phi_u(u)$  and  $\Phi_v(v)$  are velocity potentials in the  $x$  and  $y$  directions, respectively;  $V(y)$  is a position confinement potential; and  $\sigma_x$  and  $\sigma_y$  are the intensity of a white Gaussian noise providing random fluctuations. It can be shown

**Dirac  $\delta$  distribution:** special “function” that is zero when its argument is nonzero and that integrates to one

**Floor field models:** space and time discrete dynamics hinged on the transition probability to the neighboring locations

that the action in Equation 6 is equivalent to the Langevin dynamics in Equation 16, presented in Section 5. In the same section, additional details on the choice and meaning of these terms are provided.

For a Langevin dynamics, the trajectories for which  $S[\gamma]$  is stationary (i.e., those for which the variation  $\delta S[\gamma]$  vanishes) identify the trajectories observed with highest likelihood, and it is well known that the trajectories stationary for  $S[\gamma]$  solve the Euler–Lagrange equation,

$$\begin{cases} \frac{\partial \mathcal{L}}{\partial x} - \frac{d}{dt} \frac{\partial \mathcal{L}}{\partial \dot{x}} + \frac{d^2}{dt^2} \frac{\partial \mathcal{L}}{\partial \ddot{x}} = 0, \\ \frac{\partial \mathcal{L}}{\partial y} - \frac{d}{dt} \frac{\partial \mathcal{L}}{\partial \dot{y}} + \frac{d^2}{dt^2} \frac{\partial \mathcal{L}}{\partial \ddot{y}} = 0, \end{cases} \quad 7.$$

for the Lagrangian function

$$\mathcal{L}(\ddot{x}, \dot{x}, x, \ddot{y}, \dot{y}, y) = \frac{1}{2\sigma_x^2} \left( \dot{u} + \frac{\partial \Phi_u}{\partial u} \right)^2 + \frac{1}{2\sigma_y^2} \left( \dot{v} + \frac{\partial \Phi_v}{\partial v} + \frac{\partial V}{\partial y} \right)^2. \quad 8.$$

### 4.3. Generalized Floor Field Models

In general, the formulation of a crowd model via the action functional  $S$  (Equation 6) may incorporate nonlocal effects. In practice, it may be a reasonable approximation to consider situations in which some degree of locality holds. This translates into a Markov property for the full path probability:

$$\mathcal{P}(\mathbf{x}_0, \mathbf{x}_1, \dots, \mathbf{x}_N) = \mathcal{P}(\mathbf{x}_0) \cdot \prod_{j=1}^N \mathcal{P}(\mathbf{x}_j | \mathbf{x}_{j-1}), \quad 9.$$

where the factors  $\mathcal{P}(\mathbf{x}_j | \mathbf{x}_{j-1})$  encode the probability of observing a trajectory at position  $\mathbf{x}_j$  at time  $j$ , conditioned to the knowledge of the state  $\mathbf{x}_{j-1}$  at the previous time  $j - 1$ . As the velocity at time  $j$  can be computed via a finite difference of the position  $\mathbf{v}_j = \mathbf{x}_j - \mathbf{x}_{j-1}$ , considering two time instants allows one to encode the probability of both position and velocity, whereas considering three time instants also allows one to encode for the acceleration.

Statistical moments of the path integral can provide important insights into the dynamics of pedestrians; e.g., the classical heatmap (**Figure 6**) corresponds to

$$\mathcal{P}(\mathbf{c}) = \langle \delta[\mathbf{x}(t) - \mathbf{c}] \rangle_{\Gamma, t}, \quad 10.$$

where  $\mathbf{c}$  is a location on the plane, and the average is taken over the ensemble of all possible trajectories  $\gamma \in \Gamma$ , weighted by the relative probability,  $\mathcal{P}[\gamma]$  (Equation 4), and selected by the Dirac  $\delta$  distribution. Note that a trajectory  $\gamma$  can pass by  $\mathbf{c}$  at any arbitrary time  $t$ .

A floor field model (see Section 4.1) can be written as

$$\mathcal{P}(\mathbf{c} | \mathbf{c}') = \frac{\langle \delta[\mathbf{x}(t) - \mathbf{c}] \delta[\mathbf{x}(t-1) - \mathbf{c}'] \rangle_{\Gamma, t}}{\mathcal{P}(\mathbf{c}')}, \quad 11.$$

which exceeds the probability of observing a path that is at position  $\mathbf{c}$  at an arbitrary time  $t$  and at position  $\mathbf{c}'$  at time  $t - 1$ . These classical heatmap and floor map models ignore time (by integrating the probability over all times). The time dependency can easily be recovered by considering, e.g., a space-time generalization of the heatmap model,

$$\mathcal{P}(\mathbf{c}; t_j) = \langle \delta[\mathbf{x}(t) - \mathbf{c}] \delta(t - t_j) \rangle_{\Gamma, t} = \langle \delta(\mathbf{x}_j - \mathbf{c}) \rangle_{\Gamma}, \quad 12.$$

and of the floor map,

$$\mathcal{P}(\mathbf{c}|\mathbf{c}'; t_j) = \frac{\langle \delta(\mathbf{x}_j - \mathbf{c})\delta(\mathbf{x}_{j-1} - \mathbf{c}') \rangle_{\Gamma}}{\mathcal{P}(\mathbf{c}')}, \quad 13.$$

now explicitly depending on time,  $t_j$ . By not averaging over time, it is possible to observe the spatial evolution of the trajectories and how the floor map model develops under the feet of a walking pedestrian (**Figure 6**).

Limiting to one-step Markov models allows one to learn only the statistics of positions and velocities. A simple generalization of the same approach allows one to also learn the acceleration of pedestrians and, thus, inertial effects. This is done with the two-step Markov process:

$$\mathcal{P}(\mathbf{c}|\mathbf{c}', \mathbf{c}''; t_j) = \frac{\langle \delta(\mathbf{x}_j - \mathbf{c})\delta(\mathbf{x}_{j-1} - \mathbf{c}')\delta(\mathbf{x}_{j-2} - \mathbf{c}'') \rangle_{\Gamma}}{\langle \delta(\mathbf{x}_{j-1} - \mathbf{c}')\delta(\mathbf{x}_{j-2} - \mathbf{c}'') \rangle_{\Gamma}}, \quad 14.$$

which allows one to learn the probability of positions, velocities, and accelerations, e.g., discretized via finite difference. For any practical application, in all these models the space coordinate  $\mathbf{x}$  needs to be discretized, e.g., on a Cartesian lattice, using cells of linear size  $\Delta x \simeq 0.5\text{--}1$  m, the natural size of a person.

In **Figure 6a**, we show the classical heatmap,  $b(\mathbf{c}) = \mathcal{P}(\mathbf{c})$ , whereas in **Figure 6b**, we report the space-time heatmap for the same venue based on about 55 million trajectories. Although the heatmap does not provide any information on the dynamics, the space-time heatmap allows one to easily identify and extract the most common dynamical patterns. This clearly shows how the path-integral formulation allows the systematic derivation of models that can be fed with experimental data.

#### 4.4. Variational Principles

In this formulation, it is assumed that for each admissible trajectory, pedestrians choose the one that minimizes a discomfort functional (1). Similar to Fermat's principle in geometrical optics, such a functional could measure, e.g., the time to destination. In the case of light, this is equivalent to minimization of the optical length  $\int_A^B n_r ds = \int_A^B c/v ds$ , where the time to destination takes into account the fact that the speed of light in a medium with refraction index  $n_r$  is  $v = c/n_r$ . In the case of pedestrians, the estimated time to destination—keeping account of the local density  $\rho[\mathbf{x}(t)]$  that, via the fundamental diagram, yields  $v = v(\rho)$  and thus a reduction of the walking speed—satisfies  $\int_A^B dt = \int_A^B ds/v[\rho(\mathbf{x})]$ . In practice, the estimation of the time to destination will be one of several factors that can influence the choice of a path; others can be path directness, perceived comfort, and the presence of leader figures, as discussed in a modeling perspective in Reference 71 and quantitatively analyzed in Reference 72.

It is worth mentioning that Fermat's variational principle, which allows one to select the paths that minimize the discomfort, can also be rephrased via an eikonal equation for the propagation of the fronts, yielding Hughes's equations (Equations 2 and 3) for crowds (1).

### 5. MICROSCOPIC SCALE

Observing crowds at the single-pedestrian level clearly provides a richer description with respect to more macroscopic levels, and it is absolutely essential in order to improve our fundamental understanding of crowd dynamics. At this scale, a crowd of  $N$  pedestrians is addressed in a molecular dynamics-like perspective considering the positions  $\mathbf{x}_i(t) = [x_i(t), y_i(t)]$  ( $i = 1, \dots, N$ ) and velocities  $\mathbf{v}_i(t) = [u_i(t), v_i(t)]$  of all individuals. The dynamics are typically modeled as an exchange of social forces between the pedestrians (20, 88). This means that the motion is ruled by the classical

**Social force:**  
the “effective” force that explains the observed acceleration of pedestrians interacting with one another or with the environment

## Newton equation

**Non-Newtonian force:**

When two pedestrians collide, the forces experienced need not be equal and opposite, as in Newtonian mechanics

$$\sum_{\substack{j=1 \\ j \neq i}}^q \mathbf{F}_{j,i} = m_i \dot{\mathbf{v}}_i, \quad 15.$$

where the  $q$  non-Newtonian forces  $\mathbf{F}_{1,i}, \dots, \mathbf{F}_{q,i}$  act on the  $i$ th pedestrian and entail interaction with the environment, the maintenance of a (smooth) planned walking route, a comfortable speed, and the (avoidance) interaction with other pedestrians. Furthermore, if density levels increase, the range of these social forces may diminish. It is worth stressing that the social force substantially deviates from classical mechanics. First, the system does not conserve energy, as pedestrians are an example of active particles that self-propel. Second, when pedestrians interact, the sum of the forces acting on the two pedestrians does not sum to zero (i.e.,  $F_{ij} \neq F_{ji}$ ; thus, Newton's law of action and reaction does not hold), which, among others, is a direct consequence of the fact that social forces are mediated by sight and cognitive procedures (89). It is therefore clear that the expression of such a social force may be extremely complex, possibly depending upon a wide range of parameters beyond mutual positions [sight range (10), relative velocity (14, 90), time to collision or perceptions thereof] while not even satisfying linear additivity (89, 91). Finally, supermicroscopic degrees of freedom, such as body and head rotation, and cultural origin, are most likely to play a role.

Many possible effects were already included in the original social force model (20), such as propulsion guided by a desired background velocity field and (velocity-dependent) attraction and repulsion forces between pedestrians. Subsequently, much effort has been put into understanding whether and which type of social forces may reproduce some of the observed phenomenology, with corrections to the original model (20) often aimed at reproducing some macroscopic feature from newly available laboratory measurements. Emergence and time statistics of lane in counter-flows have been addressed, e.g., in Reference 10, whereas modifications to the classical social force model are proposed in Reference 92 to prevent qualitative nonphysical behavior at small densities (yet, at the price of additional parameters). Social forces for pedestrians' obstacle avoidance have been considered in References 17, 93, and 94. Specifically, Reference 94 proposed to further decompose and better specialize the avoidance force in a longitudinal deceleration force and in a transversal avoidance force (see also the comparison with experimental data in Reference 14). References 95 and 96 proposed an avoidance mechanism incorporating the prediction of future positions, whereas Reference 97 introduced a self-stopping action as an ultimate mutual avoidance mechanism that also prevents simulated pedestrians from unphysically pushing one another at high densities. Reference 98 used follow-the-leader social forces to study the impact of individuals knowledgeable about the geometry in an evacuating crowd. Various types of interactions with the environment and the geometry have also been considered: The turning behavior when facing walls was treated in Reference 99 in ordinary conditions and in Reference 100 under conditions of scarce visibility, whereas Reference 101 modeled attractive interactions with cultural elements. References 63 and 102 studied the social force model to address bottleneck dynamics reproducing the intermittency of the time lapses between successive crossings of the opening (see also **Figure 5**). Social force models have been adapted to address the presence of groups via interaction potentials (e.g., 67, 68, 70, 103, 104). Notably, overdamped limits of Equation 15 yielding first-order (i.e., velocity-based) dynamics have been studied as well (e.g., the collision-free models; 105).

The quantity and quality of experimental data are crucial for quantitative analyses and model validation—which, otherwise, can feature high uncertainty (94). Only recently, real-life measurement campaigns, extended over long time periods, allowed the acquisition of high-statistics data

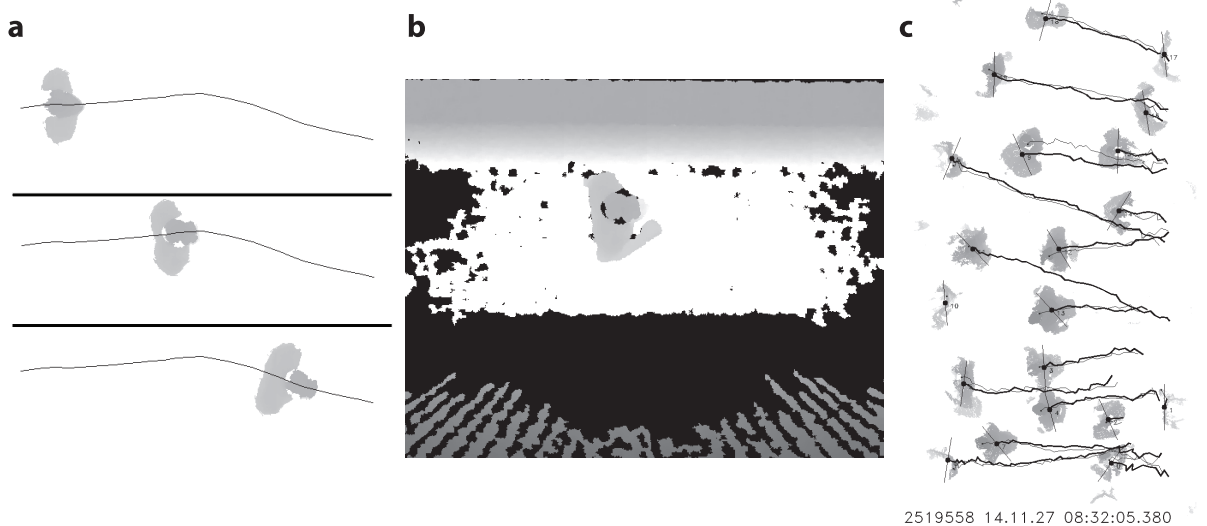


**Figure 7**

Examples of overhead depth maps collected in real-life conditions. (a,b) Pedestrian walking toward the opposite side of a corridor. (a) Three depth maps from three instants close in time. The reconstructed trajectory of the pedestrian head is superimposed as a solid line. The gray-scale colorization follows the depth levels. Darker pixels are closer to the camera plane; thus, heads, which are local extrema of the depth field, are darkest. The background, immutable in time, has been subtracted. (b) Example of a raw depth map for the middle frame in panel a. Pixels whose depth could not be assessed reliably by the sensor are in black. These typically include far-background pixels or shaded regions. (c) Higher-density depth-based tracking at a train station in Eindhoven, The Netherlands (17, 38). Panels a and b adapted from Reference 106; copyright 2017 American Physical Society. Panel c adapted from Reference 17.

allowing fully fledged statistical comparisons of pedestrian dynamics and social force models including average behaviors, fluctuations, and rare events, yet in relatively simple conditions, as outlined in the next sections.

### 5.1. Pedestrians Dynamics in the Diluted Limit

The dynamics of individual pedestrians, even when walking undisturbed and along straight paths (Figure 7a,b), possibly the simplest condition, displays a rather surprising phenomenology (Figure 8). Reference 106 showed that the dynamics of a single pedestrian can be modeled in terms of a social force that helps keep a pedestrian on their intended walking path. Together with a noise term allowing one to introduce inter- and intrapersonal variabilities around an average (intended) walking path, this yields a system of Langevin-like stochastic ordinary differential equations (106):

$$\begin{cases} \dot{x}(t) = u(t), \\ \dot{u}(t) = f(u) + \sigma_x \dot{W}_x, \\ \dot{y}(t) = v(t), \\ \dot{v}(t) = g(y) - 2\gamma v(t) + \sigma_y \dot{W}_y, \end{cases} \quad 16.$$

where the coordinate system is such that  $x(t)$  represents the longitudinal position along the intended walking path and  $y(t)$  represents the position transversal offset to the intended walking path. The terms  $\dot{W}_x$  and  $\dot{W}_y$  are delta-correlated and mutually uncorrelated white noise components, respectively, scaled by  $\sigma_x$  and  $\sigma_y$ . Because Equation 16 can be solved analytically when

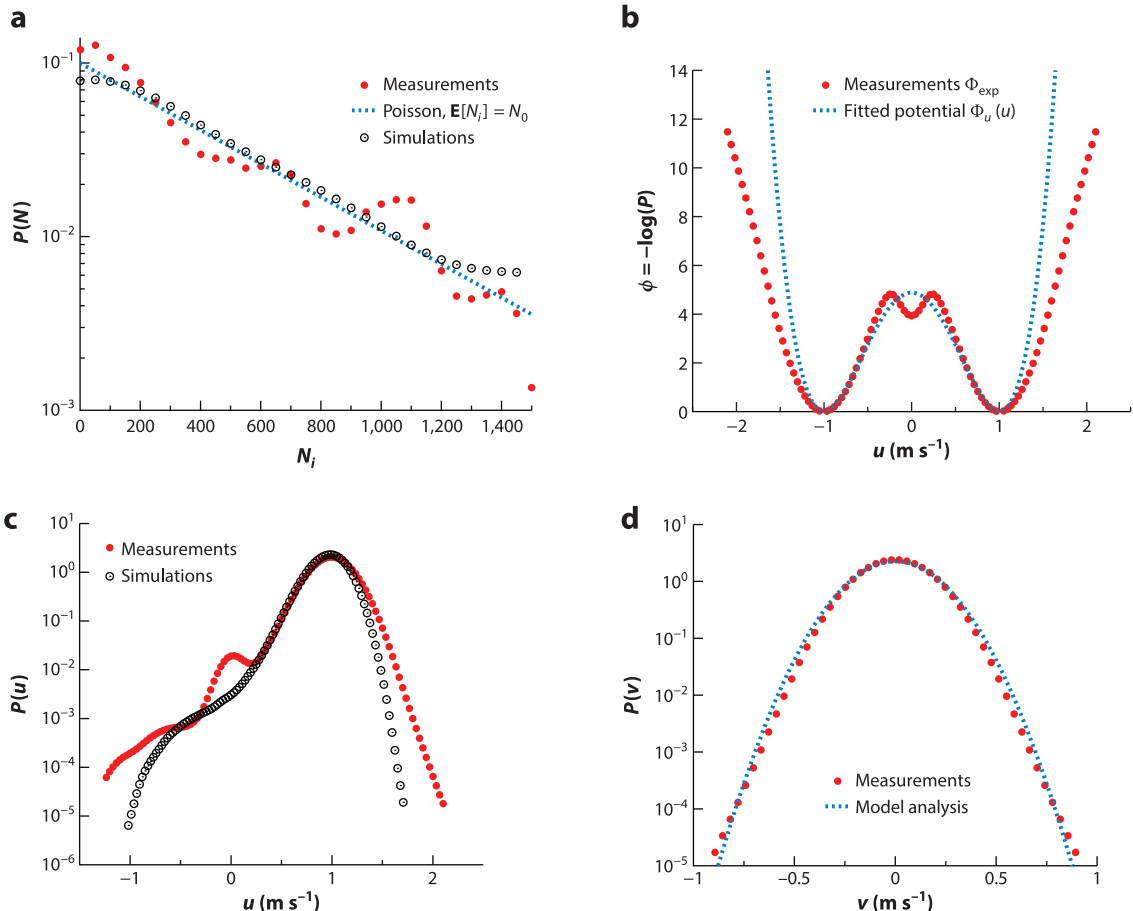


**Figure 8**

Observables of pedestrians walking undisturbed (i.e., in diluted conditions) along a straight corridor (**Figure 7a,b**): comparison of experimental data and a Langevin dynamics with a double-well velocity potential  $\Phi_u = \Phi_u(u)$  (Equation 16). (a) Probability distribution function of the number of pedestrians,  $N_i$ , between two trajectory-inversion events in diluted conditions. Comparison of measurements (red dots), simulation data from Equation 16 (black open circles), and a Poisson process with expectation  $\langle N_i \rangle = 450$  pedestrians (blue dotted line). (b) Experimental potential (after symmetrization of the velocities:  $\Phi_{\text{exp}} = -\log [P(u) + P(-u)]$ ; red dots) compared with the rescaled potential  $R\Phi_u(u) = R(u^2 - u_p^2)^2$  (dotted line). (c) Probability distribution function of longitudinal velocity  $u$ : comparison between measurements (red dots) and model (open circles). The simulated dynamics captures the entity of the fluctuation as well as the negative velocity tail within the considered approximation (high-velocity behavior and stops have been neglected). (d) Transversal velocity dynamics exhibiting a Gaussian fluctuation (similarly, it holds for the transversal position around the preferred path). Figure adapted from Reference 106; copyright 2017 American Physical Society.

the forcing terms derive from potentials (106), the longitudinal and transversal potentials can be derived from experimental probability distribution functions. Reference 106 used minimalistic models and showed that this was enough to manage quantitative accuracy. Specifically, the transversal dynamics includes a linear damping term, parameterized by the friction coefficient,  $\gamma$ , and a linear force restoring the transversal position to the intended walking path,  $y_p$ , depending on the coefficient  $\beta$ :  $g(y) = -2\beta[y(t) - y_p] = -\partial_y\beta[y(t) - y_p]^2 = -\partial_yV(y)$  [here  $y_p$  acts as a constant; i.e.,  $\dot{y}_p = 0$  (dynamics in  $y_p$  to introduce pedestrian–pedestrian interactions can be included; see Equation 17)].

The longitudinal dynamics entails the active propulsion along the intended path, and it is modeled via the term

$$f(u) = -\partial_u \Phi_u(u) = -\partial_u \alpha (u^2 - u_p^2)^2 = -4\alpha u(u^2 - u_p^2),$$

which is the gradient of a double-well velocity potential  $\Phi_u$ , i.e., containing a double minimum. Therefore, the dynamics evolves close to one of the two minima,  $u_{\min} = \pm u_p$ , corresponding to a pedestrian walking in the positive or negative  $x$  direction, respectively. It is interesting to notice that the noise term, in addition to being able to explain the observed fluctuation in the velocity, is also capable of quantitatively reproducing the (Poisson) probability of observing a pedestrian inverting the direction of motion. This feature of pedestrians reversing the direction of motion was consistently observed in other field observational experiments (17), and it appears to be a robust feature of pedestrian dynamics. **Figure 8** compares experimental measurements and the Langevin model in Equation 16 in terms of velocity inversion probability, experimental and fitted velocity potential, and longitudinal and transversal velocity probability densities.

## 5.2. Pedestrian Avoidance and Social Forces

The simple model just discussed clearly shows how stochastic differential equations can quantitatively reproduce the dynamics of pedestrians walking undisturbed. One relevant question is whether it is possible to extend this type of atomistic model to include, in quantitative and statistically accurate terms, interactions as social forces among different pedestrians.

A simple example of what a social force looks like and how it can be successful in modeling pedestrian collision avoidance was studied in Reference 17, where many collisions between individual pedestrians walking in opposite directions were observed for different initial conditions, parameterized by transversal distance along the planned path (that thus plays the role of an impact parameter). When such a parameter is much greater than the size of a single individual, we expect that pedestrians will not change their preferred path, whereas when the impact parameter approaches or is smaller than the size of a single pedestrian, corrections to the preferred paths are necessary in order to avoid collisions. The experimental data have been shown to be accurately reproduced by a rather simple generalization of the model given by Equation 16, whereby

$$g(y) = -2\beta[y - y_p(t)] = -\partial_y[y - y_p(t)]^2, \quad 17.$$

with  $y_p = y_p(t)$  being the time-dependent transversal coordinate of the intended walking path to become part of the model. During the collision process, the value of the coordinate  $y_p$  of each of the two pedestrians may change to manage mutual avoidance (**Figure 9**). This has been modeled with the following stochastic differential equation to be applied to two pedestrians (i.e.,  $j = 1, 2$ ):

$$\begin{cases} \dot{y}_p(t) = v_p(t), \\ \dot{v}_p(t) = F_{\text{vision}} - 2\mu v_p(t), \\ \dot{x}(t) = u(t), \\ \dot{y}(t) = v(t), \\ \dot{u}(t) = -4\alpha u(u^2 - u_p^2) + \sigma_x \dot{W}_x - e_x F_{\text{short}}, \\ \dot{v}(t) = -2vv - 2\beta(y - y_p) + \sigma_y \dot{W}_y - e_y F_{\text{short}} + F_{\text{vision}}, \end{cases} \quad 18.$$

where the forcing terms  $F_{\text{vision}}$  and  $F_{\text{short}}$ , which couple the pedestrians  $j = 1, 2$ , read as

$$\begin{cases} F_{\text{vision}} = -\text{sign}(e_y) A \exp(-d^2/R^2) \chi_1(\tilde{\theta}), \\ F_{\text{short}} = B \exp(-d^2/r^2) \chi_2(\tilde{\theta}), \end{cases} \quad 19.$$

where  $e_x$  and  $e_y$  are the components of the unit vector directed from  $j = 1$  and  $j = 2$ ;  $A$  and  $B$  are positive parameters;  $d$  is the (scalar) distance between the two pedestrians (**Figure 9**);  $r$  and

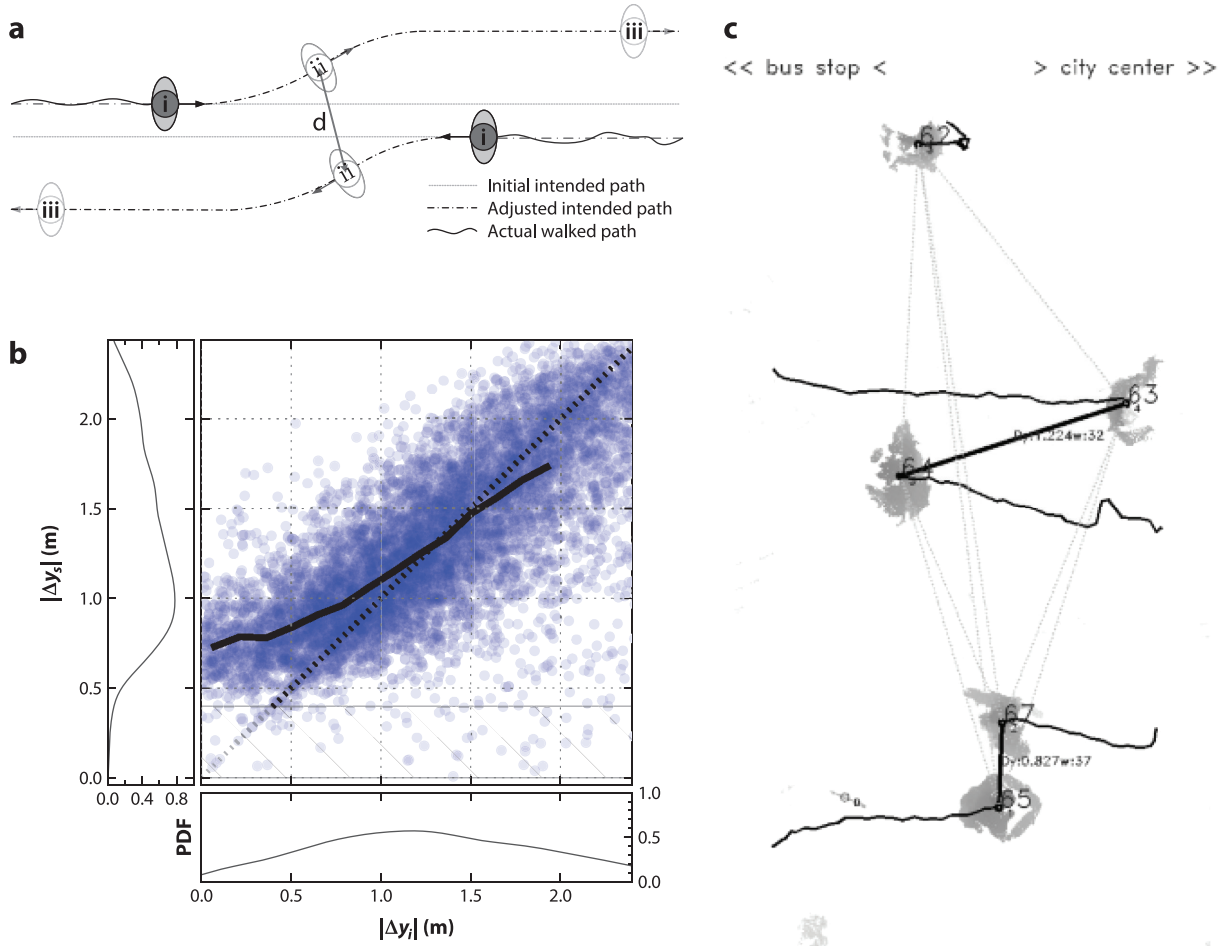


**Figure 9**

Pair-wise avoidance of pedestrians walking in opposite direction—data acquired via overhead depth tracking in the main walkway of Eindhoven Centraal station in The Netherlands (**Figure 7c**). (a) Sketch of the prototypical situation. The planned path of a pedestrian gets modified as an outcome of the interaction. (b) Experimental statistics of pairwise pedestrian distance, measured orthogonally with respect to the preferred path,  $|\Delta y|$ . The transversal distance when pedestrians enter the observation domain,  $|\Delta y_i|$ , and when they are closest in space,  $|\Delta y_s|$ , are reported, respectively, on the x and y axes. In case of pedestrians in a head-on collision,  $|\Delta y_i| \approx 0$ , the transversal distance as they bypass each other is  $|\Delta y_s| \approx 75$  cm. (c) Example of an overhead depth map including two pairwise avoidance scenarios among those contributing to the statistics in the panel b. Abbreviation: PDF, probability distribution function. Figure adapted from Reference 17; copyright 2022 American Physical Society.

$R$  are scaling factors for the interaction ranges;  $\tilde{\theta}$  is the angle between the line joining the two pedestrians and the horizontal; and  $\chi_j(\tilde{\theta}) = 1$  for  $|\tilde{\theta}| < \theta_j$  and 0 otherwise. This model is capable of quantitatively reproducing the observed collision between pedestrians (**Figure 9**).

### 5.3. The Dynamics of Pedestrian Groups

One intriguing feature about human crowd composition is the presence of groups. Typically, up to 70% of pedestrians walking in crowds belong to a social group (e.g., family or friends; 68). The dynamics of pedestrians when walking alone or within a group is clearly different: When in social

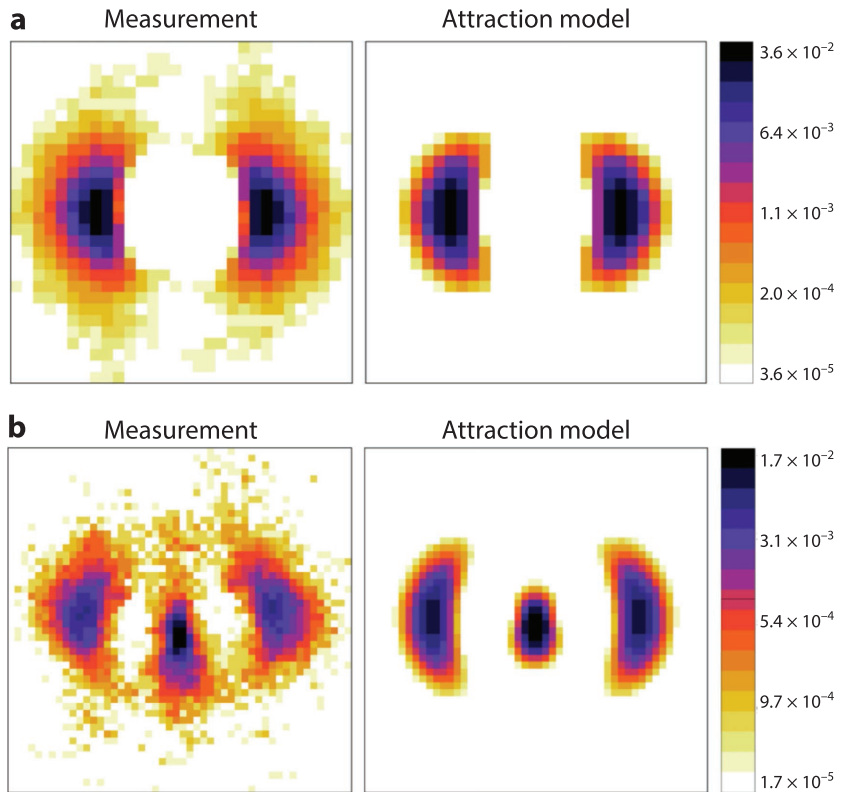


**Figure 10**

(a) Pairs of pedestrians or (b) groups of three pedestrians walking in a social group tend to keep a geometrical shape that depends on the surrounding crowd density (104). A quantitative measure has been performed in terms of the probability density of relative positions (here reported in logarithmic scale). Measurements (*left subpanels*) are compared with a social-force-based attraction model (*right subpanels*). Figure adapted with permission from Reference 107.

groups, individuals adjust their positions to maintain an acceptable (short) distance from the other group elements to enhance the possibility of communicating (68). This has been modeled as a cohesive social force restricted to group elements (70), possibly dependent on the type of group: colleagues, couples, friends, or a family (67). It is also interesting to notice that pedestrian groups assume different shapes that strongly depend upon the density of the surrounding crowd. In particular, it was observed that at low densities individuals in groups are mainly aligned transversally with respect to the direction of motion, whereas at higher densities they tend to align in a V shape (68). Accurate observational experiments have allowed the quantification of the probability distribution function of group shapes, particularly focusing on groups of two and three individuals (dyads and triads; 103, 107) (see also **Figure 10**). It is worth mentioning that, in order to study groups dynamics and their influence on the general crowd flow, it is paramount to be able to accurately identify pedestrians belonging to the same social group. This is a nontrivial task, and it has been approached either by exhaustive manual annotation (e.g., 103) or automatically, under the proxemics-driven assumption that trajectories that remain close in space over prolonged periods of time must belong to group members (19). In both cases, observation of the crowd for a longer period is essential in order to identify groups.

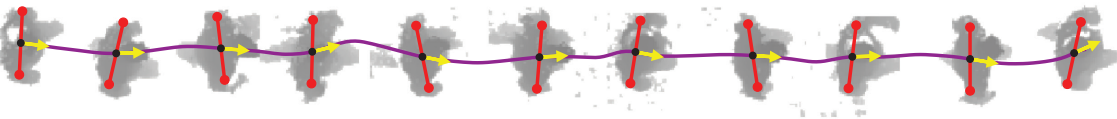


**Figure 11**

Submicroscopic measurement of shoulder orientation in depth maps. A machine-learning approach based on a deep convolutional neural network is used to determine shoulder orientation with an accuracy around  $7.5^\circ$ . Figure adapted with permission from Reference 41.

## 6. SUBMICROSCOPIC SCALE

Although it is clear that physics models can allow us to describe many of the most remarkable features of human crowds, it is also clear that describing a crowd via the position, as a function of time, of each of its individuals is a rather strong simplification. Even when considering simple parameters such as the average walking speed, one would expect this to correlate with, e.g., the height of people. Therefore, any model that is not properly informed with relevant submicroscopic details of the crowd composition (e.g., in terms of the statistical distribution of individual's heights, but also individuals' aims considering, for instance, commuters versus tourists) may not be accurate and may need fine-tuning against experimental measurements. Other important submicroscopic aspects have to do with details of the locomotion (e.g., 62, 108) and the anisotropy of pedestrians. It is clear that their dynamics is influenced mostly by what is visible, especially in diluted conditions, and by the fact that we have an elongated shape in dense conditions (63).

Estimating the crowd composition automatically is a challenging task. Besides analyses connected with height estimates or driven by manual annotators (103), the first examples of automated inferences have been proposed, e.g., the probability framework in Reference 109 that aims to estimate the type of group of two people within a finite number of predefined classes (colleagues, couples, etc.), based only on trajectories, observables, and preclassified ground truth. In general, new machine-learning-based technologies may open up novel possibilities in this direction. One example is the recent development of machine-learning approaches to record with very high accuracy the orientation of shoulders from depth-map images (41; **Figure 11**).

### SUMMARY POINTS

1. The flow of human crowds is a multiscale process characterized by emerging complexity.
2. The language of physics allows interpretation and modeling of the dynamics of crowds at different timescales and length scales.
3. Crowd composition plays an important role in understanding pedestrian dynamics.

### FUTURE ISSUES

1. Psychological factors can play a subtle and important role in the dynamics of crowds. Properly designed real-life observational experiments may allow studies of the dynamics of crowds without any artificial psychological bias.

2. Observation of crowds at the submicroscopic scales is essential to develop more accurate crowd models.
3. The combination of model-driven and data-driven approaches, e.g., by integrating the path-integral formalism with extensive experimental tracking, may allow a compromise between understanding and generality.

## DISCLOSURE STATEMENT

The authors are not aware of any affiliations, memberships, funding, or financial holdings that might be perceived as affecting the objectivity of this review.

## ACKNOWLEDGMENTS

This work is partially supported by the High Tech Systemen en Materialen research program “HTCrowd: a high-tech platform for human crowd flows monitoring, modeling and nudging,” project number 17962, of the Dutch Research Council.

## LITERATURE CITED

1. Hughes RL. 2003. *Annu. Rev. Fluid Mech.* 35:169–82
2. Marchetti MC, Joanny JF, Ramaswamy S, Liverpool TB, Prost J, et al. 2013. *Rev. Mod. Phys.* 85(3):1143–89
3. Cristiani E, Piccoli B, Tosin A. 2014. *Multiscale Modeling of Pedestrian Dynamics*, Vol. 12: *Modeling, Simulation and Applications*. Cham, Switz.: Springer
4. Bellomo N, Piccoli B, Tosin A. 2012. *Math. Models Methods Appl. Sci.* 22:1230004
5. Duives DC, Daamen W, Hoogendoorn SP. 2013. *Transp. Res. C Emerg. Technol.* 37:193–209
6. Helbing D. 2001. *Rev. Mod. Phys.* 73(4):1067–141
7. Bain N, Bartolo D. 2019. *Science* 363(6422):46–49
8. Boltes M, Seyfried A. 2013. *Neurocomputing* 100:127–33
9. Feliciani C, Nishinari K. 2016. *Phys. Rev. E* 94:032304
10. Moussaid M, Guillot EG, Moreau M, Fehrenbach J, Chabiron O, et al. 2012. *PLOS Comput. Biol.* 8(3):e1002442
11. Zhang J, Seyfried A. 2014. *Phys. A Stat. Mech. Appl.* 405:316–25
12. Zhang J, Seyfried A. 2014. In *17th International IEEE Conference on Intelligent Transportation Systems (ITSC)*, pp. 542–47. Piscataway, NJ: IEEE. <https://doi:10.1109/ITSC.2014.6957746>
13. Garcimartín Á, Parisi DR, Pastor JM, Martín-Gómez C, Zuriguel I. 2016. *J. Stat. Mech. Theory Exp.* 2016:043402
14. Seer S, Brändle N, Ratti C. 2014. *Transp. Res. C Emerg. Technol.* 48:212–28
15. Bršćić D, Zanlungo F, Kanda T. 2014. *Transp. Res. Procedia* 2:77–86
16. Bršćić D, Kanda T, Ikeda T, Miyashita T. 2013. *IEEE Trans. Human-Mach. Syst.* 43(6):522–34
17. Corbetta A, Meeusen JA, Lee C, Benzi R, Toschi F. 2018. *Phys. Rev. E* 98:062310
18. Corbetta A, Lee C, Muntean A, Toschi F. 2017. *Collect. Dyn.* 1:A10
19. Pouw CA, Toschi F, van Schadewijk F, Corbetta A. 2020. *PLOS ONE* 15(10):e0240963
20. Helbing D, Molnár P. 1995. *Phys. Rev. E* 51(5):4282–86
21. Burstedde C, Klauck K, Schadschneider A, Zittartz J. 2001. *Phys. A Stat. Mech. Appl.* 295(3/4):507–25
22. Hankin B, Wright RA. 1958. *J. Oper. Res. Soc.* 9(2):81–88
23. Predtechenskii VM, Milinskii AI. 1978. *Planning for Foot Traffic Flow in Buildings*. Washington, DC: National Bureau of Standards, US Department of Commerce, and the National Science Foundation
24. Johansson A, Helbing D, Shukla P. 2007. *Adv. Complex Syst.* 10:271–88
25. Centorrino P, Corbetta A, Cristiani E, Onofri E. 2021. *J. Comput. Sci.* 53:101357

26. Piccialli F, Yoshimura Y, Benedusi P, Ratti C, Cuomo S. 2020. *Neural Comput. Appl.* 32(12):7785–801
27. Rutten P, Lees MH, Klous S, Sloot PM. 2021. *Phys. A Stat. Mech. Appl.* 563:125448
28. van den Heuvel J, Voskamp A, Daamen W, Hoogendoorn SP. 2015. In *Proceedings of Traffic and Granular Flow*, Vol. 13, ed. M Chraibi, M Boltes, A Schadschneider, A Seyfried, pp. 73–82. Cham, Switz.: Springer
29. Adrian RJ, Westerweel J. 2011. *Particle Image Velocimetry*. Cambridge, UK: Cambridge Univ. Press
30. Baker S, Scharstein D, Lewis J, Roth S, Black MJ, Szeliski R. 2011. *Int. J. Comput. Vis.* 92:1–31
31. Baqui M, Löhner R. 2019. *IEEE Trans. Intel. Transp. Syst.* 21(2):580–89
32. Helbing D, Johansson A, Al-Abideen HZ. 2007. *Phys. Rev. E* 75:046109
33. Parisi DR, Sartorio AG, Colonnello JR, Garcimartín A, Pugnaloni LA, Zuriguel I. 2021. *PNAS* 118(50):e2107827118
34. Marsden M, McGuinness K, Little S, O'Connor NE. 2017. In *Proceedings of the 12th International Joint Conference on Computer Vision, Imaging and Computer Graphics Theory and Applications (VISIGRAPP 2017)*, Vol. 5, pp. 27–33. Setúbal, Port.: SciTePress
35. Yamamoto H, Yanagisawa D, Feliciani C, Nishinari K. 2019. *Transp. Res. B Methodol.* 122:486–510
36. Boltes M, Holl S, Tordeux A, Seyfried A, Schadschneider A, Lang U. 2016. In *Proceedings of Pedestrian and Evacuation Dynamics 2016*, ed. W Song, J Ma, L Fu, pp. 540–47. Hefei, China: Univ. Sci. Technol. China
37. Seyfried A, Passon O, Steffen B, Boltes M, Rupprecht T, Klingsch W. 2009. *Transp. Sci.* 43(3):395–406
38. Corbetta A, Meeusen J, Lee C, Toschi F. 2016. In *Proceedings of Pedestrian and Evacuation Dynamics 2016*, ed. W Song, J Ma, L Fu, pp. 18–24. Hefei, China: Univ. Sci. Technol. China
39. Kroneman W, Corbetta A, Toschi F. 2020. *Collect. Dyn.* 5:33–40
40. Spaarnaj M, Duives DC, Hoogendoorn SP. 2020. In *Traffic and Granular Flow 2019*, ed. I Zuriguel, A Garcimartín, RC Hidalgo, pp. 249–55. Cham, Switz.: Springer
41. Willems J, Corbetta A, Menkovski V, Toschi F. 2020. *Sci. Rep.* 10:11653
42. Boltes M, Adrian J, Raytarowski AK. 2021. *Sensors* 21(6):2108
43. Zhang J, Mehner W, Holl S, Boltes M, Andresen E, et al. 2014. *Phys. Lett. A* 378(44):3274–77
44. Weidmann U. 1992. *Transporttechnik der Fussgänger: Transporttechnische Eigenschaften des Fussgängerverkehrs, Literaturnauswertung*. Tech. Rep., ETH Zürich
45. Feliciani C, Murakami H, Nishinari K. 2018. *PLOS ONE* 13(12):e0208496
46. Seyfried A, Steffen B, Klingsch W, Boltes M. 2005. *J. Stat. Mech. Theory Exp.* 2005:P10002
47. Chattaraj U, Seyfried A, Chakraborty P. 2009. *Adv. Complex Syst.* 12(3):393–405
48. Zeng G, Schadschneider A, Zhang J, Wei S, Song W, Ba R. 2019. *Phys. Lett. A* 383(10):1011–18
49. Vanumu LD, Ramachandra Rao K, Tiwari G. 2017. *Eur. Transp. Res. Rev.* 9:49
50. Frisch U, Kolmogorov AN. 1995. *Turbulence: The Legacy of A.N. Kolmogorov*. Cambridge, UK: Cambridge Univ. Press
51. Hoogendoorn SP, Daamen W, Knoop VL, Steenbakkers J, Sarvi M. 2017. *Transp. Res. Procedia* 23:480–96
52. Flötteröd G, Lämmel G. 2015. *Transp. Res. B Methodol.* 71:194–212
53. Ye R, Chraibi M, Liu C, Lian L, Zeng Y, et al. 2019. *J. Stat. Mech. Theory Exp.* 2019:043401
54. Lian L, Mai X, Song W, Richard YKK, Wei X, Ma J. 2015. *J. Stat. Mech. Theory Exp.* 2015:P08024
55. Zhang J, Klingsch W, Schadschneider A, Seyfried A. 2011. *J. Stat. Mech. Theory Exp.* 2011:P06004
56. Murakami H, Feliciani C, Nishiyama Y, Nishinari K. 2021. *Sci. Adv.* 7(12):eabe7758
57. Karamouzas I, Skinner B, Guy SJ. 2014. *Phys. Rev. Lett.* 113:238701
58. Suma Y, Yanagisawa D, Nishinari K. 2012. *Phys. A Stat. Mech. Appl.* 391(1/2):248–63
59. Zhang J, Klingsch W, Schadschneider A, Seyfried A. 2012. *J. Stat. Mech. Theory Exp.* 2012:P02002
60. Zhang J, Klingsch W, Schadschneider A, Seyfried A. 2009. *Bidirectional flow*. Data Set, Pedestr. Dyn. Data Arch., Forsch. Jülich, Ger. <https://doi.org/10.34735/ped.2009.12>
61. Pedestr. Dyn. Data Arch. 2005. *Data archive of experimental data from studies about pedestrian dynamics*. Data Set, Pedestr. Dyn. Data Arch., Forsch. Jülich, Ger. <https://ped.fz-juelich.de/da/doku.php?id=start>
62. Jia X, Feliciani C, Yanagisawa D, Nishinari K. 2019. *Phys. A Stat. Mech. Appl.* 531:121735
63. Hidalgo RC, Parisi DR, Zuriguel I. 2017. *Phys. Rev. E* 95:042319
64. Nicolas A, Kuperman M, Ibañez S, Bouzat S, Appert-Rolland C. 2019. *Sci. Rep.* 9:105
65. Pastor JM, Garcimartín A, Gago PA, Peralta JP, Martín-Gómez C, et al. 2015. *Phys. Rev. E* 92:062817

66. Hoogendoorn SP, Daamen W. 2005. *Transp. Sci.* 39(2):147–59
67. Zanlungo F, Yücel Z, Bršćić D, Kanda T, Hagita N. 2017. *PLOS ONE* 12(11):e0187253
68. Moussaïd M, Perozo N, Garnier S, Helbing D, Theraulaz G. 2010. *PLOS ONE* 5(4):e10047
69. Nicolas A, Hassan FH. 2021. *Transp. A Transp. Sci.* <https://doi.org/10.1080/23249935.2021.1970651>
70. Zanlungo F, Ikeda T, Kanda T. 2014. *Phys. Rev. E* 89:012811
71. Hoogendoorn SP, Bovy PHL. 2004. *Transp. Res. B Methodol.* 38:169–90
72. Gabbana A, Toschi F, Ross P, Haans A, Corbetta A. 2022. *PNAS Nexus* 1(4):pgac169
73. Bittihn S, Schadschneider A. 2021. *J. Stat. Mech. Theory Exp.* 2021:033401
74. Johansson A, Helbing D, Al-Abideen HZ, Al-Bosta S. 2008. *Adv. Complex Syst.* 11(4):497–527
75. Arnold VI. 2013. *Mathematical Methods of Classical Mechanics*. New York: Springer
76. Bellomo N, Dogbe C. 2011. *SIAM Rev.* 53(3):409–63
77. Tordeux A, Lämmel G, Hänseler FS, Steffen B. 2018. *Transp. Res. C Emerg. Technol.* 93:128–47
78. Rendell P. 2016. *Turing Machine Universality of the Game of Life*. Cham, Switz.: Springer
79. Blue VJ, Adler JL. 2001. *Transp. Res. B Methodol.* 35(3):293–312
80. Rothman DH, Zaleski S. 2004. *Lattice-Gas Cellular Automata: Simple Models of Complex Hydrodynamics*. Cambridge, UK: Cambridge Univ. Press
81. Lovreglio R, Ronchi E, Nilsson D. 2015. *Phys. A Stat. Mech. Appl.* 438:308–20
82. Kirchner A, Nishinari K, Schadschneider A. 2003. *Phys. Rev. E* 67:056122
83. Feliciani C, Nishinari K. 2016. *Phys. A Stat. Mech. Appl.* 451:135–48
84. Wei-Guo S, Yan-Fei Y, Bing-Hong W, Wei-Cheng F. 2006. *Phys. A Stat. Mech. Appl.* 371(2):658–66
85. Zinn-Justin J. 2021. *Quantum Field Theory and Critical Phenomena*. Oxford, UK: Oxford Univ. Press. 5th ed.
86. Corbetta A, Toschi F. 2019. In *Complexity Science: An Introduction*, ed. M Peletier, R Van Santen, E Steur, pp. 329–45. Singapore: World Sci.
87. Dürr D, Bach A. 1978. *Commun. Math. Phys.* 60(2):153–70
88. Chraibi M, Kemloh U, Schadschneider A, Seyfried A. 2011. *Netw. Heterog. Media* 6(3):425
89. Moussaïd M, Helbing D, Theraulaz G. 2011. *PNAS* 108(17):6884–88
90. Chraibi M, Seyfried A, Schadschneider A. 2010. *Phys. Rev. E* 82:046111
91. Corbetta A, Schilders L, Toschi F. 2020. In *Crowd Dynamics, Vol. 2: Theory, Models, and Applications*, ed. L Gibelli, pp. 33–53. New York: Birkhäuser
92. Lakoba TI, Kaup DJ, Finkelstein NM. 2005. *Simulation* 81(5):339–52
93. Moussaïd M, Helbing D, Garnier S, Johansson A, Combe M, Theraulaz G. 2009. *Proc. R. Soc. B* 276:2755–62
94. Rudloff C, Matyus T, Seer S, Bauer D. 2011. *Transp. Res. Rec.* 2264:101–9
95. Zanlungo F, Ikeda T, Kanda T. 2011. *Europhys. Lett.* 93:068005
96. Xu Q, Chraibi M, Seyfried A. 2021. *Transp. Res. C Emerg. Technol.* 133:103464
97. Parisi DR, Gilman M, Moldovan H. 2009. *Phys. A Stat. Mech. Appl.* 388(17):3600–8
98. Hou L, Liu JG, Pan X, Wang BH. 2014. *Phys. A Stat. Mech. Appl.* 400(9):93–99
99. Echeverría-Huarte I, Nicolas A, Hidalgo RC, Garcimartín A, Zuriguel I. 2022. *Sci. Rep.* 12:2647
100. Xue S, Jiang R, Wong S, Feliciani C, Shi X, Jia B. 2020. *Transp. A Transp. Sci.* 16(3):626–53
101. Kwak J, Jo H, Lutinen T, Kosonen I. 2013. *Phys. Rev. E* 88:062810
102. Zuriguel I, Parisi DR, Hidalgo RC, Lozano C, Janda A, et al. 2014. *Sci. Rep.* 4:7324
103. Zanlungo F, Yücel Z, Kanda T. 2020. *Collect. Dyn.* 5:118–25
104. Zanlungo F, Bršćić D, Kanda T. 2015. *Phys. Rev. E* 91:062810
105. Xu Q, Chraibi M, Tordeux A, Zhang J. 2019. *Phys. A Stat. Mech. Appl.* 535:122521
106. Corbetta A, Lee C, Benzi R, Muntean A, Toschi F. 2017. *Phys. Rev. E* 95:032316
107. Zanlungo F, Bršćić D, Kanda T. 2014. *Transp. Res. Procedia* 2:149–58
108. Parisi DR, Negri PA, Bruno L. 2016. *Phys. Rev. E* 94:022318
109. Yucel Z, Zanlungo F, Feliciani C, Gregorj A, Kanda T. 2019. *PLOS ONE* 14(10):e0223656

# Contents

A Journey Through Nonlinear Dynamics: The Case of Temperature Gradients <i>Albert Libchaber</i> .....	1
An Adventure into the World of Soft Matter <i>Dominique Langevin</i> .....	21
Floquet States in Open Quantum Systems <i>Takashi Mori</i> .....	35
Generalized Symmetries in Condensed Matter <i>John McGreevy</i> .....	57
Non-Hermitian Topological Phenomena: A Review <i>Nobuyuki Okuma and Masatoshi Sato</i> .....	83
Modeling Active Colloids: From Active Brownian Particles to Hydrodynamic and Chemical Fields <i>Andreas Zöttl and Holger Stark</i> .....	109
Spin Seebeck Effect: Sensitive Probe for Elementary Excitation, Spin Correlation, Transport, Magnetic Order, and Domains in Solids <i>Takashi Kikkawa and Eiji Saitoh</i> .....	129
Superconductivity and Local Inversion-Symmetry Breaking <i>Mark H. Fischer, Manfred Sigrist, Daniel F. Agterberg, and Youichi Yanase</i> .....	153
Tensor Network Algorithms: A Route Map <i>Mari Carmen Bañuls</i> .....	173
Spatial and Temporal Organization of Chromatin at Small and Large Scales <i>Helmut Schiessel</i> .....	193
Dissecting Flux Balances to Measure Energetic Costs in Cell Biology: Techniques and Challenges <i>Easun Arunachalam, William Ireland, Xingbo Yang, and Daniel Needleman</i> .....	211
Data-Driven Discovery of Robust Materials for Photocatalytic Energy Conversion <i>Arunima K. Singh, Rachel Gorelik, and Tathagata Biswas</i> .....	237

Fermiology of Topological Metals <i>A. Alexandradinata and Leonid Glazman</i>	261
Physics of Human Crowds <i>Alessandro Corbetta and Federico Toschi</i>	311
Random Quantum Circuits <i>Matthew P.A. Fisher, Vedika Khemani, Adam Nahum, and Sagar Vijay</i>	335
Swimming in Complex Fluids <i>Saverio E. Spagnolie and Patrick T. Underhill</i>	381
Learning Without Neurons in Physical Systems <i>Menachem Stern and Arvind Murugan</i>	417
Quantum Many-Body Scars: A Quasiparticle Perspective <i>Anushya Chandran, Thomas Iadecola, Vedika Khemani, and Roderich Moessner</i>	443
Odd Viscosity and Odd Elasticity <i>Michel Fruchart, Colin Scheibner, and Vincenzo Vitelli</i>	471

## Errata

An online log of corrections to *Annual Review of Condensed Matter Physics* articles may be found at <http://www.annualreviews.org/errata/conmatphys>